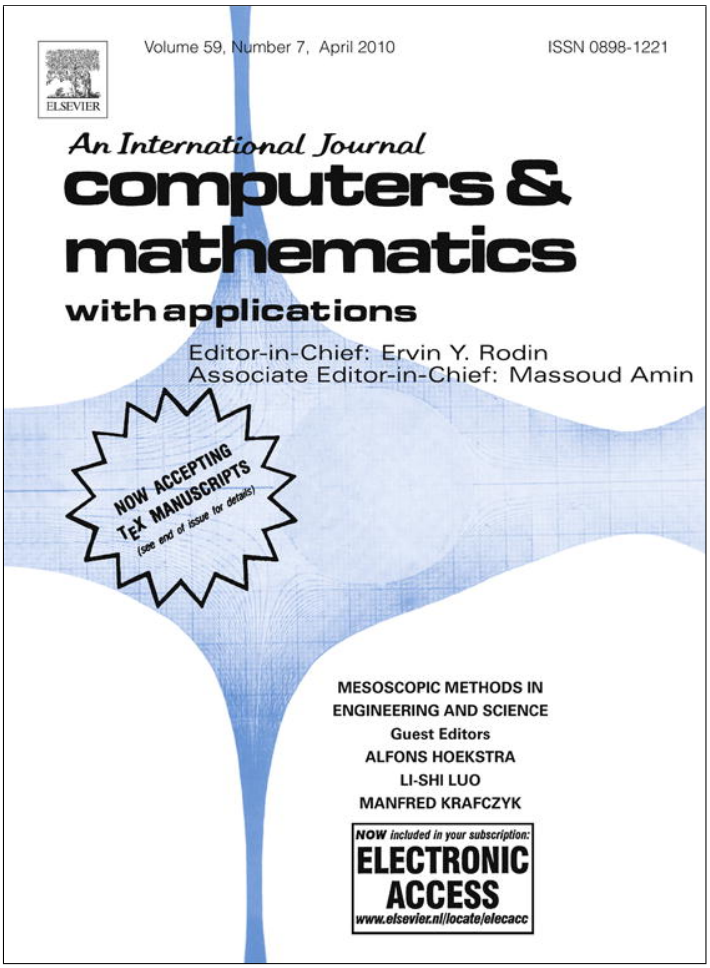

Computers and Mathematics with Applications 59 (2010) 2290–2304

Contents lists available at ScienceDirect

Computers and Mathematics with Applications

journal homepage: www.elsevier.com/locate/camwa

Viscous flow and colloid transport near air–water interface in a microchannel

Xiao-yan Shi [a], Hui Gao [a], Volha I. Lazouskaya [b], Qinjun Kang [c], Yan Jin [b], Lian-Ping Wang [a,*]

[a] Department of Mechanical Engineering, University of Delaware, Newark, DE 19716, USA
[b] Department of Plant and Soil Sciences, University of Delaware, Newark, DE 19716, USA
[c] Los Alamos National Laboratory, Los Alamos, NM 87545, USA

ARTICLE INFO

Keywords:
Gas–liquid interfacial flow
Moving contact line
Colloid retention
Colloid transport
Lattice Boltzmann equation
Interface tracking

ABSTRACT

In order to understand the transport behavior of colloids near an air–water interface (AWI), two computational methods are applied to simulate the local water flow field near a moving AWI in a 2D microfluidic channel. The first method is a mesoscopic multicomponent and multiphase lattice Boltzmann (LBM) model and the second is the macroscopic, Navier–Stokes based, volume-of-fluid interface tracking method. In the LBM, it is possible to predict the dynamic contact angles after the static contact angle is correctly set, and the predicted dynamic contact angles are in good agreement with previous observations. It is demonstrated that the two methods can yield a similar flow velocity field if they are applied properly. The flow field relative to AWI depends on the direction of the flow, and exhibits curved streamlines that transport fluid between the center of the channel and the wall region. Using the obtained flow, the motion of sub-micron colloids in a de-ionized water solution is then studied by a Lagrangian approach. The observed colloid trajectories are in qualitative agreement with our visualizations using a confocal microscope.

1. Introduction

An improved understanding of the mechanisms governing colloid retention and transport in soil porous media is crucial to the management of groundwater contamination by strongly sorbing contaminants or by pathogens such as viruses, bacteria, and protozoa [1,2]. Since contaminants and colloids often originate near the land surface, colloid transport and retention in unsaturated soil (i.e., the vadoze zone) are affected by air–water and air–water–solid interfaces. The air–water interface (AWI) may act as a colloid carrier [3,4] or a dynamic physical barrier to transport [5]. The moving contact lines can serve as the site for colloid retention [6,7] or act to re-mobilize colloids previously deposited on grain surface [8]. Lazouskaya et al. [9] reviewed the complex processes associated with colloid transport and retention near AWI, and stressed the need to understand the microscale flow field and the need to examine together the hydrodynamic transport and physicochemical interactions near the moving AWI.

To better understand the mechanisms of colloid transport and retention near AWI and moving contact line, we shall develop a computational approach to address the following aspects: (1) the simulation of viscous flow involving an air–water interface and (2) the tracking of colloids in such a flow field in the presence of AWI and grain surface.

* Corresponding author.
E-mail addresses: graceshi@udel.edu (X.-y. Shi), hgao@udel.edu (H. Gao), volha@udel.edu (V.I. Lazouskaya), qkang@lanl.gov (Q. Kang), yjin@udel.edu (Y. Jin), lwang@udel.edu (L.-P. Wang).

0898-1221/$ – see front matter © 2009 Elsevier Ltd. All rights reserved.
doi:10.1016/j.camwa.2009.08.059

In recent years, a significant progress has been made in developing computational methods for multiphase interfacial flows. Different methods are available to treat the fluid–fluid interface, including volume-of-fluid interface tracking, front tracking, level set, and lattice Boltzmann method [10–13]. These methods are still undergoing rapid development and severe numerical challenges remain, such as numerical instability for large density/viscosity ratios and spurious currents. Most methods are designed to simulate the shape of fluid–fluid interface. Relatively less attention is paid to the detailed flow velocity field near the fluid–fluid interface.

As a first step, in this paper we consider a viscous flow with a moving fluid–fluid interface in a 2D microfluidic channel. The characteristics of the flow are mostly governed by low capillary number and low flow Reynolds number, namely, the fluid inertial force may be neglected and the flow is mainly governed by viscous force and surface tension. We shall apply simultaneously two computational methods to solve the fluid flow: a mesoscopic multicomponent and multiphase lattice Boltzmann (LBM) model [10] and a macroscopic, Navier–Stokes based, volume-of-fluid interface tracking (VOFIT) method [11]. LBM is better suited for simulating moving contact lines while VOFIT has better numerical stability for large density and viscosity ratios. Our first objective is to simulate the flow field in the fluid–fluid interfacial region as accurately as possible. A good inter-comparison between the two methods would serve as a good indication that such an objective is achievable.

Our second objective is to simulate the motion of colloids in the interfacial region and to compare the colloid trajectories with our parallel experimental observations reported in [9]. For this purpose, Lagrangian tracking of colloids is developed by numerically integrating the colloid's equation of motion with physicochemical, hydrodynamic, Brownian and body forces. It will be demonstrated that the simulated trajectories are in good agreement with our experimental observations.

2. Flow simulation

Here we describe briefly the two computational methods used to simulate the slow viscous flow in a 2D microscale channel with a moving AWI. In our parallel experimental investigation [9], the flow is governed by a very low flow Reynolds number, about $O(10^{-4})$ on the water side and $O(10^{-5})$ on the air side, based on the mean speed $U(\sim 10\ \mu m/s)$ and the channel width ($\sim 40\ \mu m$). The capillary number $Ca = U\mu/\sigma$ on the water side is $O(10^{-9})$, where μ is the water viscosity and $\sigma = 0.072$ N/m is the surface tension at the air–water interface. Matching exactly these small physical parameters are difficult in the simulations. We shall assume that the flow near the air–water interface is similar as long as $Ca \ll 1$ and the dynamic contact angle is correctly simulated. In this paper, only a 2D model channel with a moving air–water interface is considered (e.g., see Fig. 4).

2.1. The lattice Boltzmann method

The multicomponent, multiphase, mesoscopic lattice Boltzmann method (LBM) developed by Kang et al. [14–16] is used here to simulate the flow with a moving air–water interface. The method is based on the original LBM scheme by Shan and Chen [17,18]. Since the method has been documented fully in [14–16], we only describe the method very briefly. The particular 2D code used here is a modified version of the code used in [15].

The starting point of the Shan–Chen multiphase multicomponent LBM scheme is to introduce a separate particle density distribution function $f_i^k(\mathbf{x}, t)$ for each component k, the LBM equation for the component k is

$$f_i^k(\mathbf{x} + \mathbf{e}_i\delta_t, t + \delta_t) - f_i^k(\mathbf{x}, t) = -\frac{f_i^k(\mathbf{x}, t) - f_i^{k(\mathrm{eq})}(\mathbf{x}, t)}{\tau_k}, \tag{1}$$

where τ_k is the relaxation time of the kth component, $f_i^{k(\mathrm{eq})}(\mathbf{x}, t)$ is the corresponding equilibrium distribution function. We use the standard D2Q9 lattice so $i = 0, 1, 2, \ldots, 8$ and $\mathbf{e}_i$ denotes the corresponding particle velocities in lattice unit: $\mathbf{e}_0 = (0, 0)$, $\mathbf{e}_1 = (1, 0)$, $\mathbf{e}_2 = (0, 1)$, $\mathbf{e}_3 = (-1, 0)$, $\mathbf{e}_4 = (0, -1)$, $\mathbf{e}_5 = (1, 1)$, $\mathbf{e}_6 = (-1, 1)$, $\mathbf{e}_7 = (-1, -1)$, and $\mathbf{e}_8 = (1, -1)$. The density and velocity of the kth component are obtained by

$$\rho_k = \sum_i f_i^k, \qquad \rho_k \mathbf{u}_k = \sum_i f_i^k \mathbf{e}_i. \tag{2}$$

The equilibrium velocity u_k^{eq} is determined by

$$u_k^{\mathrm{eq}} = \frac{\sum_k \rho_k \mathbf{u}_k/\tau_k}{\sum_k \rho_k/\tau_k} + \frac{\tau_k}{\rho_k}\mathbf{F}_k, \tag{3}$$

where $\mathbf{F}_k = \mathbf{F}_{1k} + \mathbf{F}_{2k}$ represents the net force due to mesoscopic fluid–fluid interaction $\mathbf{F}_{1k}$ and mesoscopic fluid–solid interaction $\mathbf{F}_{2k}$.

The key element of the scheme is the specification of the interaction force terms. The fluid–fluid interaction force is specified as

$$\mathbf{F}_{1k} = -\psi_k(\mathbf{x}) \sum_{\mathbf{x}'} \sum_{\hat{k}} G_{k\hat{k}}(\mathbf{x}, \mathbf{x}') \psi_{\hat{k}}(\mathbf{x}')(\mathbf{x}' - \mathbf{x}), \tag{4}$$

namely, the interaction force between the kth component and the $\hat{k}$th component is assumed to be proportional to the product of their *effective number density* ϕ_k defined as a function of particle local number density. Typically, only the nearest and next-nearest lattice neighbors are considered to form the set of $\mathbf{x}'$. The choice of $\mathbf{x}'$ and the relative weights $G_{k\hat{k}}$ must be made to satisfy symmetry and accuracy requirements [19]. For the D2Q9 lattice model, Kang et al. [14] suggests that

$$G_{k\hat{k}}(\mathbf{x}, \mathbf{x}') = \begin{cases} g_{k\hat{k}}, & |\mathbf{x} - \mathbf{x}'| = 1, \\ 0.25 g_{k\hat{k}}, & |\mathbf{x} - \mathbf{x}'| = \sqrt{2}, \\ 0, & \text{otherwise.} \end{cases} \tag{5}$$

The effective density ϕ_k is taken as ρ_k as in Kang et al. [15]. Other choices will lead to a different equation of state, and may be desirable for simulating high density ratio mixture and for better control of spurious velocity near the air–water interface [20]. At lattice points next to the channel wall, the fluid–fluid interaction force perpendicular to the wall is set to zero.

At the fluid–solid interface, the wall is treated as a phase with a constant density. The fluid–solid interaction force is described as

$$\mathbf{F}_{2k} = -\rho_k(\mathbf{x}) \sum_{\mathbf{x}'} g_{kw} \rho_w(\mathbf{x}')(\mathbf{x}' - \mathbf{x}), \tag{6}$$

where ρ_w is a prescribed constant particle density of the wall, which is only nonzero at the wall, and g_{kw} is the interaction strength between the kth fluid and the wall. The wettability or contact angle can be adjusted by the values of g_{kw}: a positive value simulates a nonwetting fluid and a negative value for wetting fluid [14–16].

It is important to note that the Chapman–Enskog expansion procedure can be used to derive the macroscopic continuity and momentum equation of the fluid mixture, with an effective density $\rho = \sum_k \rho_k$ and effective velocity $\mathbf{u} = \left[\sum_k \rho_k \mathbf{u}_k + 0.5 \sum_k \mathbf{F}_k\right] / \rho$ [21]. The usual Navier–Stokes equation can be derived with a pressure field for the mixture as $p = \frac{1}{3}\rho + 1.5 \sum_k \sum_{\hat{k}} g_{k\hat{k}} \psi_k \psi_{\hat{k}}$. The local fluid kinematic viscosity has a value of $\nu = \frac{1}{3} \sum_k (\rho_k \tau_k / \rho - 0.5)$. An effective surface tension can be obtained by matching the pressure distribution near the interfacial region with the Laplace law [14].

A modification we made to the Kang et al.'s code concerns the implementation of the inlet and outlet boundary conditions. In the original code the equilibrium distribution for a prescribed velocity profile is used. We found that such a simple implementation causes a pressure jump at the inlet and outlet. We instead use the method proposed by Chang et al. [22]. Their basic idea is to model a boundary node as an effective forcing. If we take, for example, the inlet boundary condition in D2Q9 lattice, we have, for each component,

$$\rho = f_0 + f_1 + f_2 + f_3 + f_4 + f_5 + f_6 + f_7 + f_8 \tag{7}$$

$$\rho u = f_1 + f_5 + f_8 - f_3 - f_6 - f_7 \tag{8}$$

$$\rho \mathrm{v} = f_2 + f_5 + f_6 - f_4 - f_7 - f_8. \tag{9}$$

At the inlet, f_1, f_5, and f_8 are not known and solved by setting

$$f_1 = f_1^* + \frac{1}{9} Q_x \tag{10}$$

$$f_5 = f_5^* + \frac{1}{36}(Q_x + Q_y) \tag{11}$$

$$f_8 = f_8^* + \frac{1}{36}(Q_x - Q_y) \tag{12}$$

where $\mathbf{Q}$ is a forcing vector. Substituting these into Eqs. (7)–(9), we have 3 equations for 3 unknowns ρ, Q_x, and Q_y. The first term, f_i^*, is taken to be the value before streaming. Solving the above, we have

$$\rho = \frac{1}{1-u}[f_0 + f_2 + f_4 + 2(f_3 + f_6 + f_7)] \tag{13}$$

$$f_1 = f_1^* + \frac{2}{3}\rho u + \frac{2}{3}(f_3 - f_1^* + f_6 - f_8^* + f_7 - f_5^*) \tag{14}$$

$$f_5 = f_5^* + \left(\frac{\rho u}{6} + \frac{\rho \mathrm{v}}{2}\right) + \frac{f_3 - f_1^*}{6} + \frac{f_4 - f_2}{2} - \frac{f_6 - f_8^*}{3} + \frac{2f_7 - 2f_5^*}{3} \tag{15}$$

$$f_8 = f_8^* + \left(\frac{\rho u}{6} - \frac{\rho \mathrm{v}}{2}\right) + \frac{f_3 - f_1^*}{6} - \frac{f_4 - f_2}{2} + \frac{2f_6 - 2f_8^*}{3} - \frac{f_7 - f_5^*}{3}. \tag{16}$$

The above procedure then completely specifies the unknown distributions at the inlet in terms of the given velocity profile. The similar procedure is used at the outlet. For the solid walls, the mid-link bounce-back scheme was used with fluid lattice nodes located half lattice spacing away from the walls, yielding a second-order accuracy of the no-slip boundary condition.

2.2. Navier–Stokes based VOFIT method

For inter-comparison purposes, we also apply a Volume-of-Fluid Interface Tracking (VOFIT) method developed by Zaleski and co-workers [11,23]. Since the approach has been extensively documented in open literature [11,23–25], we only describe the basic conceptual ingredients of the method.

In the VOFIT method, a single whole-field, macroscopic Navier–Stokes equation is solved, with a variable density and viscosity. The surface tension is modeled as a smoothed forcing term in the Navier–Stokes equation. In VOFIT, a simple fixed uniform grid is used to represent the fluid velocity field. In recent years, the VOFIT has been a method of choice for treating viscous flows with fluid–fluid interface.

The two central elements of VOFIT are the interface reconstruction/advection and the representation of surface tension by a continuous surface stress or surface force method. First, the interface reconstruction and advection is based on the idea that any portion of an interface can be approximated by a line segment in 2D (or a plane surface segment in 3D) whenever the interface is cutting through a cell. Such line segment can be uniquely determined by the interface normal and cell volume fraction. For this reason, the interface reconstruction procedure is named as piecewise linear interface calculation (PLIC). A scalar phase identification field C (volume fraction) is defined for each fixed grid cell. For example, C is set to 1 if a cell is fully occupied by the liquid phase and 0 if the cell is fully occupied by the gas phase. Interface cells are partially filled by the liquid phase, so C represents the percentage of the cell area occupied by the liquid phase.

The steps involved in the interface reconstruction and advection are: (1) if C at the time step t^n in each cell is known, the gradient field ∇C can be estimated using C values in the neighboring cells. Then C and ∇C in the current cell can be used to define a line segment approximating the interface in the cell. The step solves the inverse problem of determining a Lagrangian object (the interface) from the Eulerian C field. (2) This Lagrangian object (line segments) is then advected by the local velocity field at time step t^n. The two end points of a line segment rest on the cell boundaries before advection. After advection, the location of the two end points are known. The advected line segments form the new interface, from which the new cell volume fraction C^{n+1} can be calculated. This step is then the forward problem of determining the new Eulerian cell volume fractions from the current Lagrangian object of line segments.

In summary, the interface reconstruction makes use of the Eulerian volume fraction field only, the advection makes use of the calculated velocity field. There are quite a few subtle numerical issues in both the inverse and forward steps. A small CFL number is needed to ensure the accuracy of whole interface tracking and advection scheme.

By the end of step (2), we have a new volume fraction field as well as the new interface location, which can be used to formulate the surface tension stress or force to be included in the Navier–Stokes equation, that will then be used to advance the velocity field. Various smoothing operations have been proposed for the surface tension stress or force, to ensure numerical stability. The calculated forcing term is then incorporated into the time integration of the Navier–Stokes equation on a staggered grid using the projection method [23].

For the case of moving contact line, we specify the contact angle on the wall of the fluid–fluid interface by an extrapolation method, as discussed in [24].

2.3. Inter-comparison of the simulated flows

In the following, we provide inter-comparisons of the simulated flows in a 2D channel of width H and length L. The flow is directed in the x direction, and the channel walls are located at $y = 0$ and $y = H$.

2.3.1. Single-phase flow in a 2D channel

As a first step to compare the two multiphase flow simulation methods, we describe below a comparison of the two codes for a single-phase flow setting. It can be shown that both methods reduce to a single-phase flow setting if the surface tension and interphase interactions are turned off.

The flow to be simulated is the following. Initially the fluid is at rest in the channel. A time-dependent flow velocity profile is specified, at both the inlet and outlet, as

$$u(x = 0, y, t) = u(x = L, y, t) = 4V_0 f(t)\frac{y(H - y)}{H^2}, \tag{17}$$

$$\mathrm{v}(x = 0, y, t) = \mathrm{v}(x = L, y, t) = 0, \tag{18}$$

where V_0 is the steady-state centerline velocity of the parabolic profile. So flow is suddenly started at inlet and outlet, with the specified amount of fluid is pushed in at the inlet and the same amount taken out at the outlet.

Since by design, VOFIT is a completely incompressible code (infinite sound speed since a global Poisson equation is solved for pressure), while LBM is weakly compressible (a sound speed of $1/\sqrt{3}$ in the lattice unit), care is needed to set up the flow

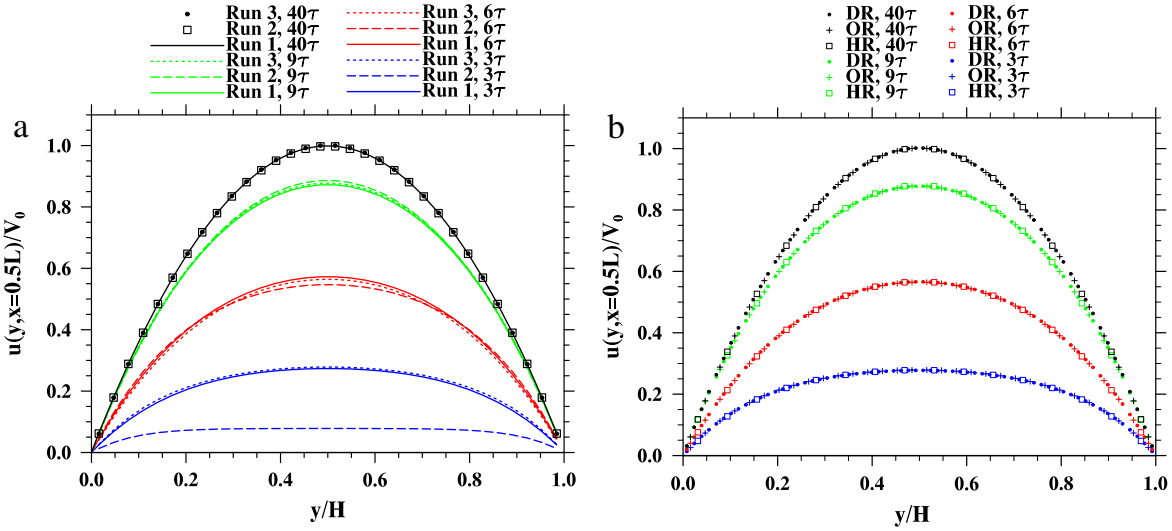

Fig. 1. Streamwise velocity profile at the middle of the channel ($x = 0.5L$). (a) Comparison of VOFIT and LBM runs; (b) comparison of LBM runs at three different resolutions (OR is the same as Run 3 shown in Table 1 with resolution 32×256, HR used half the resolution 16×128, and DR denotes a double resolution run with 64×512).

Table 1
Setup of parameters of single-phase base flow simulations.

	Symbol	Run 1, VOFIT	Run 2, LBM	Run 3, LBM
Channel width	H	1.0	32	32
Channel length	L	8.0	256	256
Fluid density	ρ	1.0	1.0	1.0
Kinematic viscosity	ν	0.1	1/6	1/30
Maximum inlet velocity	V_0	0.192	0.01	0.002
Reynolds number	$\mathrm{Re} = HV_0/\nu$	1.92	1.92	1.92
Channel length	L/H	8	8	8
Time scale	$T = H/V_0$	5.2083	3200	16000
Time scale ratio		1	614.4	3072
Time step	$\mathrm{d}t$	1/614.4	1.0	1.0
Initial transition steps		1000	1000	5000
Print time steps	N_t	100	100	500
Total time steps		4000	4000	20,000
Time interval	$\tau = N_t \mathrm{d}tV_0/H$	0.03125	0.03125	0.03125

problem properly in LBM, namely, the acoustic-wave time scale must be separated from the hydrodynamic (Navier–Stokes) flow. A transition function $f(t)$ is inserted above to ease the initial physical *singularity* of the problem:

$$f(t) = \frac{t}{T_0} \quad \text{if } 0 < t < T_0, \tag{19}$$

$$f(t) = 1.0 \quad \text{if } t > T_0. \tag{20}$$

Three runs shown in Table 1 are compared: one is VOFIT run and two LBM runs with different flow time scales. The grid resolution is set to $L = 256\delta$ and $H = 32\delta$, where δ is the grid spacing. The flow Reynolds number based on V_0 is 1.92. Fig. 1(a) shows the streamwise velocity distribution at $x = 0.5L$, at 4 different times. Several important observations can be made. First, Run 3 (LBM) and Run 1 (VOFIT) give almost identical results at all times. This shows that the acoustic-wave time scale in Run 3 is much smaller so the macroscopic flow is essentially incompressible. In Run 2 (LBM), the weak compressibility affects the initial transient evolution, causing the centerline velocity lack behind at very early times. At intermediate times, say, $t = 9\tau$ in Fig. 1(a), the velocity for Run 2 at the center could exceed the steady-state value. At long times, all three runs set down to the specified inlet/outlet profiles and the flow is no longer time dependent. To make sure that the grid resolution is sufficient, we made two additional runs with a resolution equal to half and twice that used for Run 3, the results from these LBM runs at three resolutions are shown in Fig. 1(b). Clearly, results from the three resolutions are identical so the lattice resolution is not an issue here.

Fig. 2(a) shows the streamwise velocity as a function of the streamwise distance, at $y = 0.25H$. Once again, Run 1 and Run 3 yield almost identical results. While the compressibility effect in Run 2 causes variations in the x direction. Fig. 2(b) shows the y-component velocity as a function of streamwise distance, at $y = 0.25H$. The spikes near the inlet and outlet are similar for Run 1 and Run 3. These spikes are asymmetric, as expected. They eventually disappear at the steady state. Again Run 2 shows a different distribution.

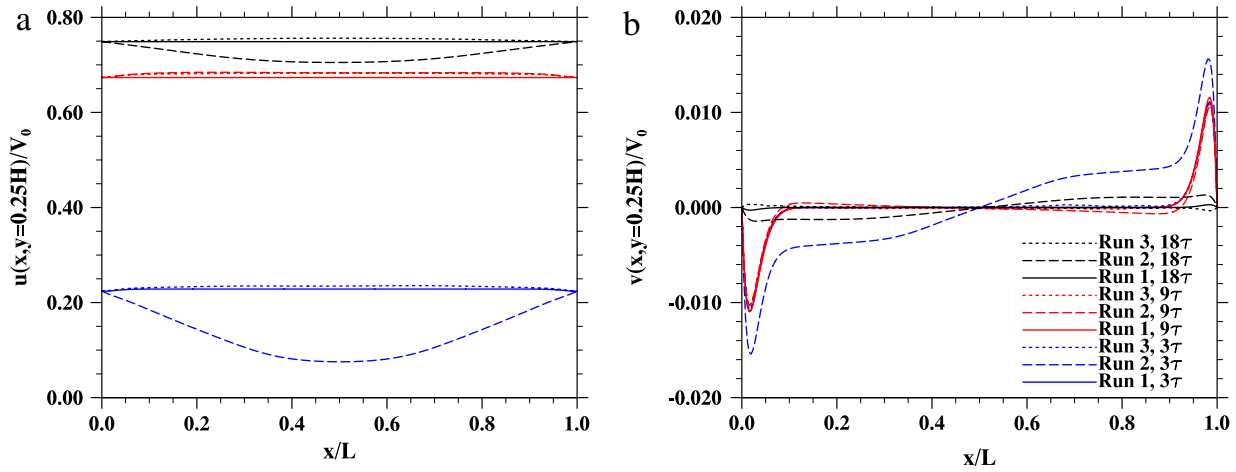

Fig. 2. (a) Streamwise velocity profile along the x axis at $y = 0.25H$. (b) Cross-channel velocity along the x axis at $y = 0.25H$.

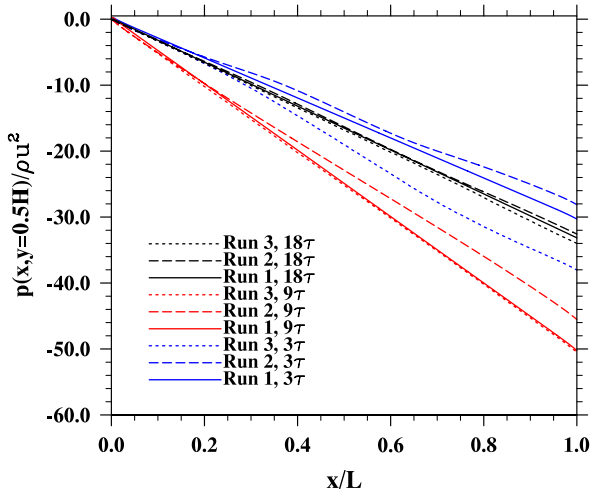

Fig. 3. Pressure distribution along the x axis at $y = 0.5H$.

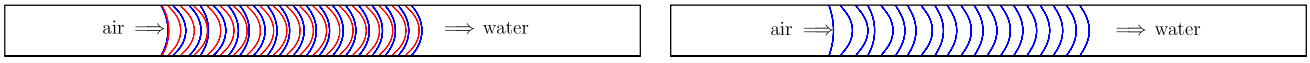

(a) LBM (Blue), VOFIT (Red). (b) LBM-DR.

Fig. 4. Time evolution of the simulated air–water interface. The blue lines represent the LBM results and the red lines VOFIT. The time instants shown are $t = m\Delta t$ with $m = 1, 2, \ldots, 20$, and $\Delta t = 0.26H/V_f$, where V_f is the steady-state advance speed of the interface and $V_f = \frac{2}{3}V_0$. Initially, the interface is located at $x = 0.25L$. (For interpretation of the references to colour in this figure legend, the reader is referred to the web version of this article.)

Finally, Fig. 3 shows the pressure distribution. The pressure is adjusted to zero at the inlet and then normalized by ρV_0^2. Clearly, all runs converge to the same linear distribution at long times. The LBM codes have different distribution at the early times due to the weak compressibility effects.

In summary, the two completely different simulation codes are used to simulate an idealized transient flow problem in a channel. The results compare well as long as the macroscopic flow time scale is made much larger than the pressure-wave time scale (in LBM). This serves as an important starting point for the inter-comparison of multiphase flow simulations in the 2D channel, to be discussed next.

2.3.2. Two-phase flow with a moving interface in 2D channel

Now we consider a moving fluid–fluid interface in the channel. The initial condition and the inlet/outlet conditions are the same as in the last section. The interface is assumed to be located at $x = 0.25L$ at $t = 0$. The densities of the two fluids are assumed to be the same, and a same viscosity is also assumed. This is done as the current versions of LBM and VOFIT codes are unable to handle large density and viscosity ratios due to numerical instability and/or large spurious currents near the fluid–fluid interface [15,20].

The parameters of the LBM code are set to reproduce a similar static contact angle of an air–water interface. For this purpose, we set $g_{1w} = -g_{2w} = 0.06$, which yield a long-time static (i.e., $V_0 = 0$) contact angle of about $67° \pm 5°$. This is

Table 2
Setup of parameters for interfacial flow simulation.

	Symbol	VOF	LBM	LBM-DR
Channel width	H	1.0	64	128
Channel length	L	8.0	800	1600
Fluid density	ρ	1.0	1.0	1.0
Kinematic viscosity	ν	0.01	0.1	0.2
Maximum inlet velocity	V_0	0.1601	0.025	0.025
Average front velocity	V_f	0.1067	0.016667	0.016667
Reynolds number	$\mathrm{Re} = HV_f/\nu$	10.67	10.67	10.67
Channel length	L/H	8	12.5	12.5
Time scale	$T = H/V_f$	9.372	3840	7680
Time scale ratio		1	409.73	819.46
Time step	$\mathrm{d}t$	0.004881	1.0	1.0
Initial transition steps		500	1000	2000
Print time steps	N_t	500	1000	2000
Total time steps		10,000	20,000	40,000
Time interval	$\tau = N_t \mathrm{d}tV_f/H$	0.26042	0.26042	0.26042
Surface tension	σ	0.05081	0.0794	0.0866
Capillary number	$Ca = V_f\mu/\sigma$	0.021	0.021	0.038
Contact angle	θ	70°	∼70°	∼70°

comparable to the observed static contact angle for an air–water interface, which ranges from 68° to 75°. When we turn on the flow, a dynamic moving interface is simulated.

We first consider the case of flow directed from the air side to the water side, the case to be referred to as the air front case. The fluid viscosity and surface tension are set to yield $Ca = 0.021$ and $\mathrm{Re} = 10.67$ (see Table 2). These parameters do not match the parameters in our microfluidic experiment. Since $Ca \ll 1$, the simulated flow is mostly governed by the surface tension and as such is believed to be qualitatively similar to the experiment. For a straight channel considered here, the flow Reynolds number is only of secondary importance. Other parameters in LBM are shown in Table 2.

Fig. 4(a) shows the locations of the interface at different times. It can be seen that the interface movement reaches a steady state when $t > 2H/V_f$, where V_f is the steady-state advance speed of the interface. Due to the very low capillary number, no fingering is developed [15]. The dynamic contact angle is measured to be about 53°, matching nicely the experimentally observed receding contact angle of 53° [9]. The shape and evolution of the interface are in good agreement with our confocal microscope observation [9].

We then specify the same dynamic contact angle in the VOFIT code. The time evolution of the shape and location of the interface is also shown in Fig. 4(a). It is evident that the steady state is developed faster in VOFIT due to absence of any compressibility effect, as discussed in the previous section. The long-time interface evolution is very similar in these two simulations. The minor difference between the LBM and VOFIT runs is due to several reasons: the compressibility in LBM affects the location of the interface; the dynamic angle specified in the VOFIT code contains measurement uncertainty of the result from the LBM code; and the VOFIT wall boundary implementation could introduce minor errors on the final interface shape. Note that the steady-state advancing speed of the air–water interface is identical as required by the inlet/outlet boundary conditions. Since we are interested in the long-time flow relative to the interface, the difference in the absolute interface location is not important.

Once again, we run another LBM simulation at double resolution (case LBM-DR shown in Table 2). In this case, we used the parameters $g = 0.25$ and $g_{1w} = -g_{2w} = 0.03$ to roughly match the shape and contact angle of the dynamic interface. The time evolution of the interface is shown in Fig. 4(b).

Next and more important, we compare the velocity field near the interface in Fig. 5. The presence of the interface alters the far-field parabolic velocity profile. The moving contact line represents a physical singularity, where a finite slip velocity relative to the wall is possible [26]. The fluid on the air side near the center of the channel has to slow down, and that near the wall has to accelerate. As a result, the fluid velocity on the left of the interface has a component directed toward the wall. The opposite occurs on the water side and the fluid moves transversely toward the center to re-establish the far-field parabolic velocity profile. LBM and VOFIT yield very similar velocity field.

We shall now provide some quantitative comparison of the velocity fields from the two numerical methods. Fig. 6(a) shows the streamwise velocity along the center of the channel ($y = 0.5H$), as a function of x/δ measured from the interface. The two methods agree quantitatively and yield very similar width of the interfacial region, as defined by the deceleration and then acceleration dip. The shape at the tip or the interface location is somewhat different, with LBM giving a sharp tip and VOFIT giving a round tip. This could be due to the smoothed surface tension volumetric force field used in VOFIT. No explicit numerical smoothing is used in LBM. This comparison is encouraging, and to our knowledge, has not been made between these two methods. The profiles from LBM and LBM-DR match well, showing that the grid resolution used is adequate.

Fig. 6(b) compares the streamwise velocity at $y = 0.25H$. While the velocity magnitude away from the interfacial region is in good agreement, the distributions in the interfacial region differ. On the air side, the LBM yields a larger deceleration. On the water side, there is a qualitative difference, with LBM showing deceleration and VOFIT showing acceleration downstream of the interface. It is noted that the magnitude of the fluctuation is relatively small.

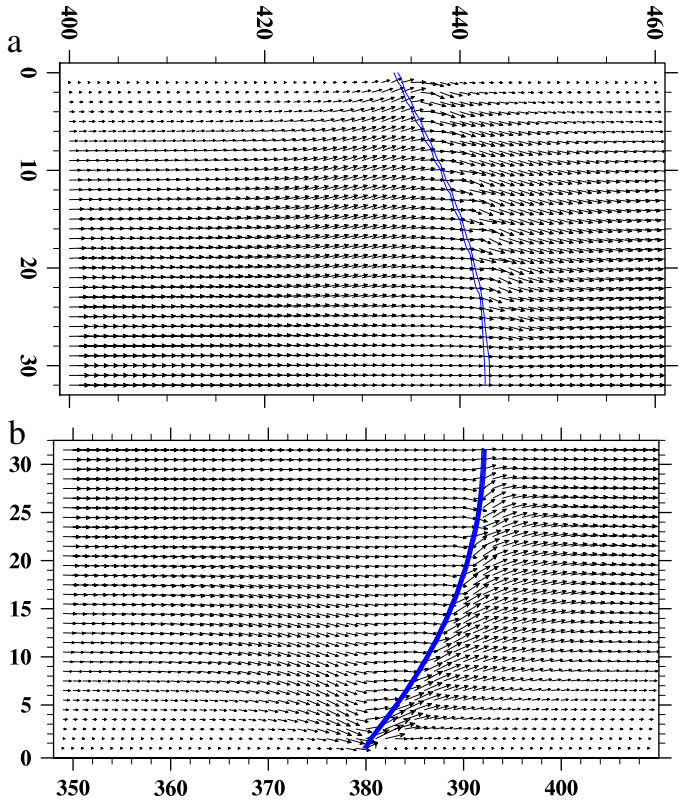

Fig. 5. The velocity field near the air–water interface: (a) VOFIT, (b) LBM. Due to the symmetry, only half of the channel is shown.

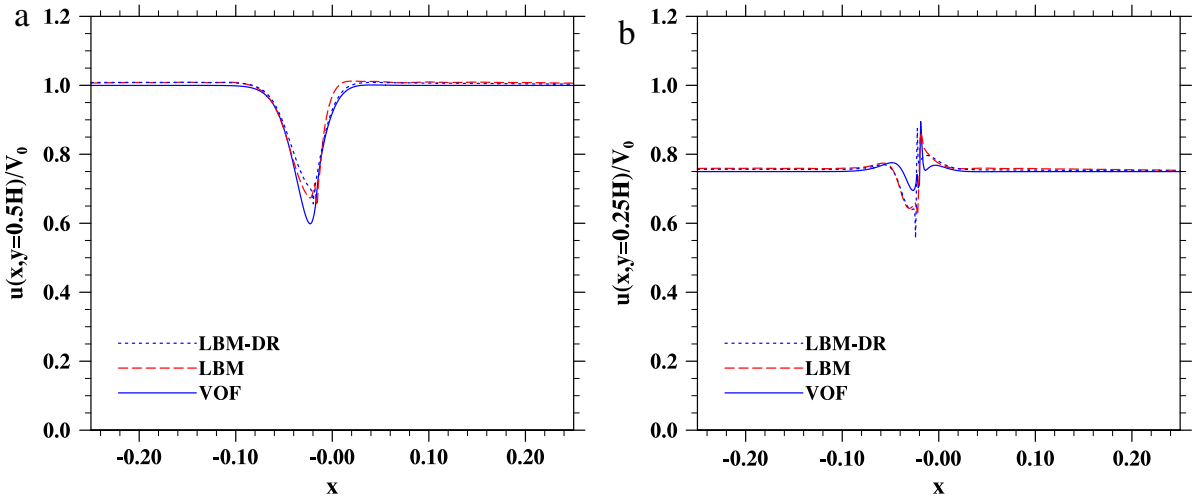

Fig. 6. Comparison of u velocity at (a) $y = 0.5H$ and (b) $y = 0.25H$.

The y-component velocity at $y = 0.25H$ is compared in Fig. 7. Overall, the profiles in the interfacial region are in reasonable agreement, with transverse flow toward the wall before the interface and toward the center after the interface. The width of the interfacial region is also quite similar. VOFIT shows a less sharp change across the interface, again perhaps due to the local smoothing operation.

We also simulated the case where the flow is directed from the water side to the air side, referred to as the water front case. The same parameter setting as the air front case is used, except the flow direction is reversed. Fig. 8 shows the time evolution of the interface and its shape from LBM simulation. Again the steady interface shape is obtained when $t > 2H/V_f$. Since this is the advancing contact line, the contact angle is large and measured to be about $77° \pm 5°$. This dynamic contact angle is again comparable to the experimentally observed advancing contact angle of about 79° [9]. The shape and evolution of the interface are in reasonable agreement with the experimental observation in [9].

For the transport of colloids relative to the air–water interface, we are interested in the velocity field relative to the interface, that is, the resulting flow field after the mean flow speed is subtracted. This relative velocity fields are shown for both the air front case and water front case in Fig. 9. For the purpose of gauging the magnitude of the spurious velocity field,

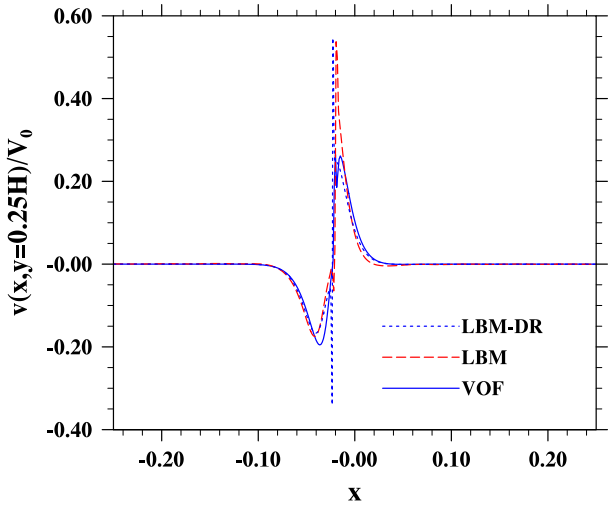

Fig. 7. Comparison of V velocity at $y = 0.25H$.

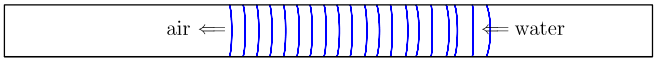

Fig. 8. Time evolution of the air–water interface when the flow is directed from the water to air. The time instants shown are $t = m\Delta t$ with $m = 1, 2, \ldots, 20$ and $\Delta t = 0.26H/V_f$. Initially, the interface is located at $x = 0.75L$.

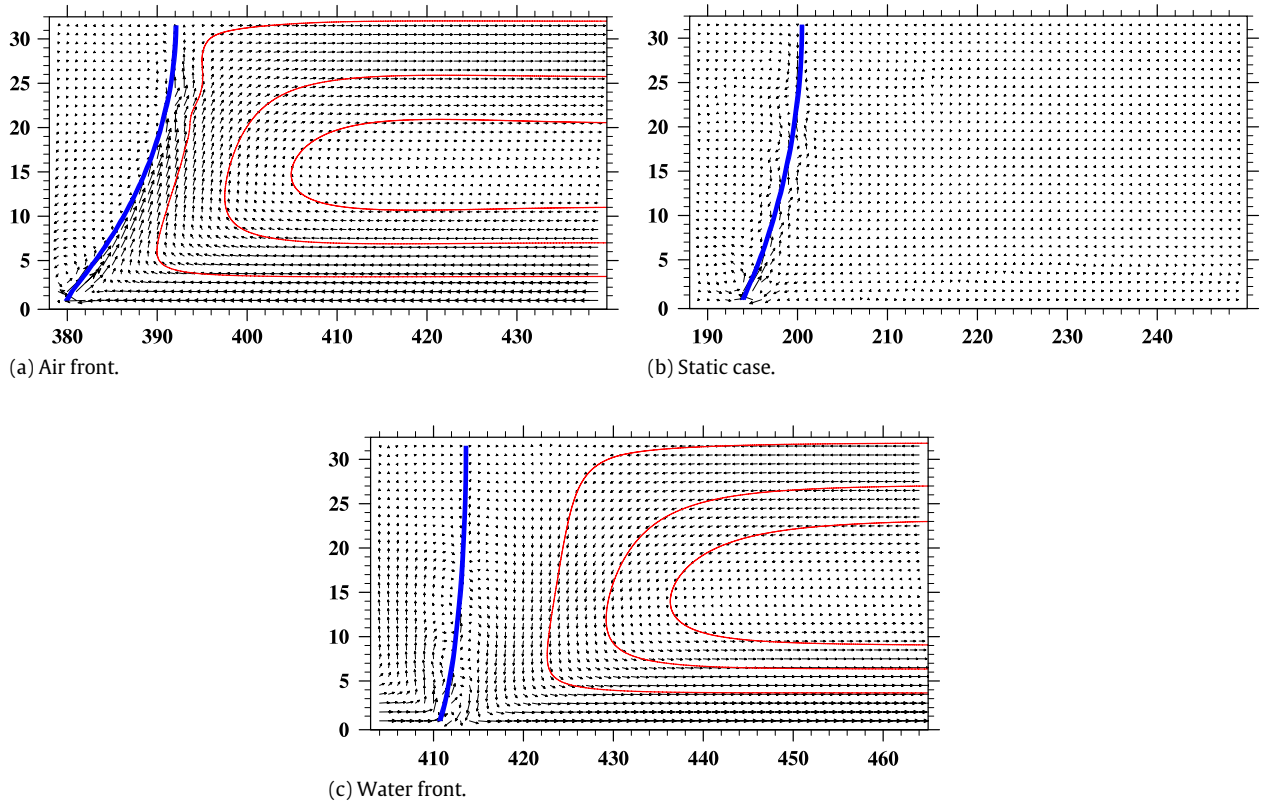

(a) Air front. (b) Static case.

(c) Water front.

Fig. 9. The velocity field on the water side observed in a frame of reference moving with the air–water interface. In (a) three streamlines starting at (440, 3.2), (440, 7), (440, 11) are shown. In (c) three streamlines starting at (465, 31.7), (465, 21), (465, 23) are plotted.

we also show in Fig. 9 the case of static contact line (i.e., $V_0 = 0$). All the relative flows are obtained using LBM simulations. An identical scaling is used for the three vector fields. Due to the symmetry of simulated flow, only half of the channel near the interface is shown. For the air front case, the relative flow on the water side is pointing away from the interface near the center of the channel, but pointing into the interface near the wall. The opposite is observed for the water front case, where now the water near the center moves into the interface and the water near the wall moves away from the interface. Fig. 9(b) demonstrates that the magnitude of spurious current is very small away from the air–water interface, but becomes

significant right at the interface. Therefore, the simulated relative flows are physical, except in region very close to the interface. Spurious current is a numerical artifact due to the discrete representation of the particle–particle interaction or surface tension force, and it is known to occur in both LBM and VOFIT.

Also shown in Fig. 9(a) and (c) are a few streamlines. These streamlines were accurately obtained by a fourth-order Runge–Kutta method using a small integration time step. One could see a very minor effect of the spurious current near AWI on the streamline closest to AWI in Fig. 9(a) for the air front case. For the water front case (Fig. 9(c)), the streamline started very close to the center of the channel turns at a noticeable distance before reaching the AWI. From these plots, the effect of spurious currents on colloid trajectories could be neglected.

3. Transport of colloids

In the remainder of the paper, we discuss briefly the trajectories of small colloids in the simulated viscous flow near the air–water interface. It is assumed that the simulated flow field relative to the interface provides a reasonable representation of the experimental water flow near the interface, after the width of the channel and the mean speed are matched with the experimental conditions reported in [9]. Here we used a physical channel width of 40 μm and a mean speed of 10 μm/s. In the following, we take a frame of reference moving with the air–water interface. Then the flow field is steady when the steady air–water interface shape and movement are established.

3.1. Equation of motion for colloids

Colloids of a radius $a_c = 0.25$ μm are followed by solving the following equation of motion:

$$m_c \frac{\mathrm{d}\mathbf{V}(t)}{\mathrm{d}t} = \mathbf{F}^{\mathrm{drag}} + \mathbf{F}^{\mathrm{b}} + \mathbf{F}^{\mathrm{g}} + \mathbf{F}^{\mathrm{B}} + \mathbf{F}^{\mathrm{c}}, \tag{21}$$

$$\frac{\mathrm{d}\mathbf{Y}(t)}{\mathrm{d}t} = \mathbf{V}(t) \tag{22}$$

where $\mathbf{V}(t)$ is the instantaneous (Lagrangian) velocity of the colloid, $\mathbf{Y}(t)$ is the instantaneous location of the colloid, $m_c \equiv 4\pi\rho_c a_c^3/3$ is the mass of the colloid, and ρ_c is the material density of the colloid. All relevant physical parameters and their corresponding values are compiled in Table 3. The hydrodynamic forces included are the quasi-steady drag force $\mathbf{F}^{\mathrm{drag}}$ and the buoyancy force $\mathbf{F}^{\mathrm{b}}$. $\mathbf{F}^{\mathrm{g}}$ is the gravitational body force. $\mathbf{F}^{\mathrm{B}}$ is a random force designed to simulate Brownian motion of the colloid due to local thermal fluctuations of solvent molecules. Finally, $\mathbf{F}^{\mathrm{c}}$ represents interaction forces of the colloid with the air–water interface or the wall (made of polymethyl methacrylate or PMMA polymer [9]).

The Stokes drag force is expressed as

$$\mathbf{F}^{\mathrm{drag}} = \zeta\left[\mathbf{u}(\mathbf{Y}(t), t) - \mathbf{V}(t)\right], \quad \text{with } \zeta \equiv 6\pi\mu a_c, \tag{23}$$

where $\mathbf{u}(\mathbf{x}, t)$ is the fluid velocity field, and μ is the fluid viscosity. In this preliminary study, local hydrodynamic interaction is not considered.

The buoyancy force and body force together is given as

$$\mathbf{F}^{\mathrm{bg}} = \mathbf{F}^{\mathrm{b}} + \mathbf{F}^{\mathrm{g}} = m_c\left(1 - \frac{\rho_w}{\rho_c}\right)\mathbf{g}, \tag{24}$$

where ρ_w is the solvent density and $\mathbf{g}$ is the gravitational acceleration.

The Brownian force is specified as $\mathbf{F}^{\mathrm{B}} = (F_1^{\mathrm{B}}, F_2^{\mathrm{B}}, F_3^{\mathrm{B}})$, where each component F_i^{B} is an independent Gaussian random variable of zero mean and the following standard deviation

$$\sigma_{F_i^{\mathrm{B}}} = \sqrt{\frac{2\zeta kT}{\mathrm{d}t}}, \tag{25}$$

where dt is the time step size, T is the temperature and k is the Boltzmann constant. When a simple explicit Euler scheme is applied, the Brownian force would generate the desired mean square value (kT/m_c) of velocity fluctuation in each direction [27].

The colloidal interaction force is only relevant when a colloid is very close to the air–water interface (AWI) or the wall. It consists of the electrostatic, van der Waals, and hydrophobic forces [28,29],

$$F^{\mathrm{c}} = F^{\mathrm{EDL}} + F^{\mathrm{vdW}} + F^{\mathrm{HP}}, \tag{26}$$

where all interaction forces are assumed to act in the direction normal to a surface, with a positive value indicating a repulsive force and negative an attractive force. The electrostatic double layer (EDL) force results from the interaction of

Table 3
Physical parameters used in the colloid equation of motion.

	Symbol	Value
Water density	ρ	1000 kg/m^3
Water viscosity	μ	0.001 kg/(m.s)
Channel width	H	40 μm
Mean speed	V_f	10 μm/s
Colloid radius	a_c	0.25 μm
Colloid density	ρ_c	1055 kg/m^3
Time step	dt	5.14×10^{-5} s
Mass of colloid (actual)	m_c	1.381×10^{-16} kg
Mass of colloid (assumed)	m_c^*	1.381×10^{-13} kg
Response time (actual)	τ_c	1.47×10^{-8} s
Response time (assumed)	τ_c^*	1.47×10^{-5} s
Flow time scale	H/V_f	4 s
Temperature	T	293 K
Boltzmann constant	k	1.38×10^{-23} J/K
Dielectric constant	ϵ	80
The medium permittivity	ϵ_0	8.842×10^{-12} C^2/Nm^2
Valence	z_0	1
Electron charge	e	1.6×10^{-19} C
The EDL thickness	κ^{-1}	2.48×10^{-7}
Surface potential of colloid	ψ_1	−0.0656 V
Colloid–AWI interaction:		
Surface potential of AWI	ψ_2	−0.065 V
Hamaker constant	A	-1.2×10^{-20} J
hydrophobicity constant	K_{132}	1.48×10^{-22} J
Colloid–wall interaction:		
Surface potential of wall	ψ_3	−0.025 V
Hamaker constant	$\hat{A}$	3.2×10^{-21} J
Hydrophobicity constant	$\hat{K}_{132}$	1.74×10^{-26} J
Colloid–colloid interaction:		
Hamaker constant	$\tilde{A}$	5.2×10^{-21} J
Hydrophobicity constant	$\tilde{K}_{132}$	2.19×10^{-28} J

a charged particle with the ions in the liquid medium and the charge at air–liquid boundary. For colloid–AWI interaction, the EDL force may be written as [9]

$$F^{\mathrm{EDL}} = 64\pi\epsilon\epsilon_0\kappa a_c \left(\frac{kT}{z_0 e}\right)^2 \tanh\left(\frac{z_0 e\psi_1}{4kT}\right) \tanh\left(\frac{z_0 e\psi_2}{4kT}\right) \exp(-\kappa h) \tag{27}$$

where h is the minimum gap between the colloid and the AWI, ϵ is the dielectric constant, ϵ_0 is the medium permittivity, z_0 is the valence, e is the electron charge, κ^{-1} is the electrical double layer thickness dependent on the solution ionic strength, and ψ_1 and ψ_2 are the surface potential (zeta potential) of the colloid and AWI, respectively.

The van der Waals force between a colloid and AWI is expressed as [30]

$$F^{\mathrm{vdW}} = -\frac{Aa_c}{6h^2}\left(\frac{1}{1+14a_c/\lambda}\right), \tag{28}$$

where A is the Hamaker constant and λ is the characteristic wavelength taken as 100 nm.

The hydrophobic force between a colloid and AWI is expressed as [29]

$$F^{\mathrm{HP}} = -\frac{a_c K_{132}}{6h^2}, \tag{29}$$

where K_{132} is the hydrophobicity constant for the interaction of a colloid with AWI.

All the parameters are listed in Table 3. The colloid–wall interaction forces are treated similarly as the colloid–AWI interaction, except that (1) the wall surface potential ψ_3 is used to replace the AWI surface potential ψ_2, (2) The Hamaker constant $\hat{A}$ for colloid–wall interaction should be used in the van der Waals force, and (3) the hydrophobicity constant is different (Table 3).

For colloid–colloid interactions, the different interactions forces are written as [29–31]

$$F^{\mathrm{EDL}} = 32\pi\epsilon\epsilon_0\kappa a_c \left(\frac{kT}{z_0 e}\right)^2 \left[\tanh\left(\frac{z_0 e\psi_1}{4kT}\right)\right]^2 \exp(-\kappa h), \tag{30}$$

$$F^{\mathrm{vdW}} = -\frac{\tilde{A}a_c}{12h}\frac{1}{(1+11.12h/\lambda)}\left[\frac{1}{h}+\frac{1}{\lambda}\frac{11.12}{(1+11.12h/\lambda)}\right], \tag{31}$$

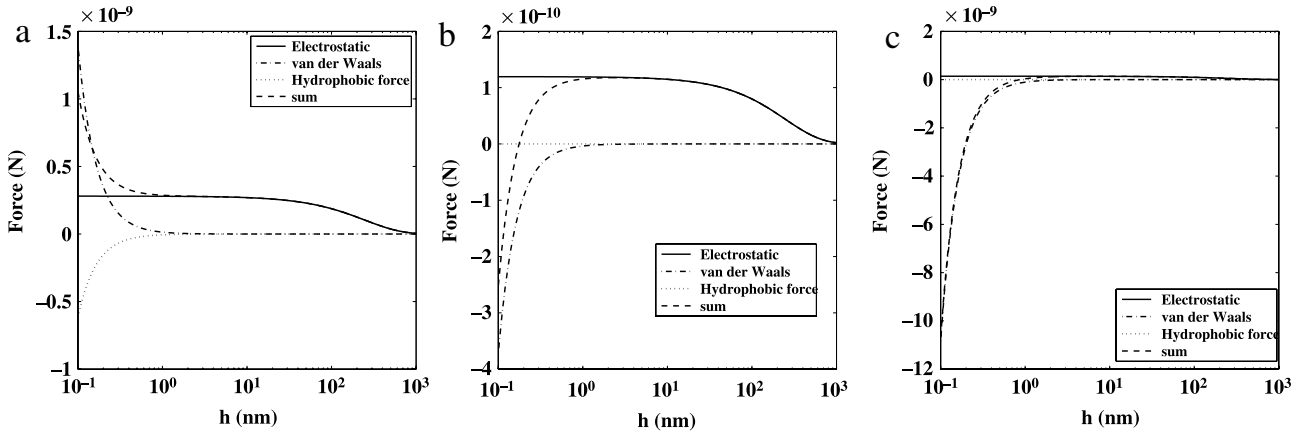

Fig. 10. Colloid–surface/colloid interface interaction forces as a function of gap distance h: (a) colloid–AWI interaction; (b) colloid–wall interaction; (c) colloid–colloid interaction. The inset in (c) shows a zoom-in view near $h = 1$ nm.

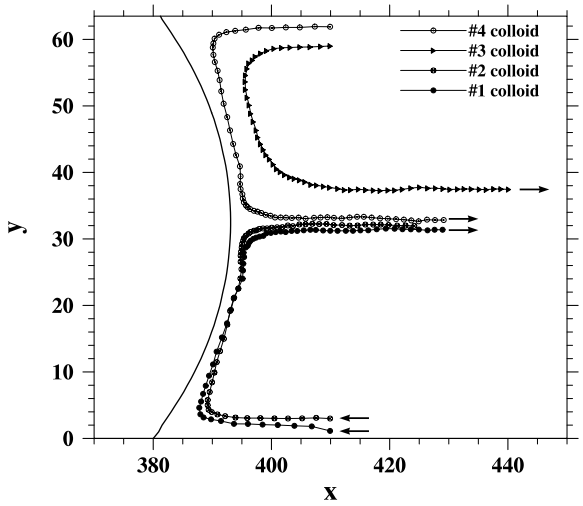

Fig. 11. Colloids' trajectory near AWI for the air front case.

$$F^{\mathrm{HP}} = -\frac{a_c \tilde{K}_{132}}{12h^2}, \tag{32}$$

where the new Hamaker constant and hydrophobicity constant are listed in Table 3.

The resulting colloidal interaction force with AWI for hydrophilic, carboxylate-modified colloids is repulsive, as shown in Fig. 10 (a). Since the solution considered here is de-ionized water which has a negligible ionic strength (10^{-6} M), the electrostatic double layer thickness is as large as 248 nm. Therefore, the repulsive electrostatic force is dominant at the separation distances larger than 1 nm. At closer separation distances, the calculated van der Waals force along with hydrophobic force take over with overwhelming magnitude compared to the electrostatic force. Note that the Hamaker constant for colloid–AWI interaction is negative, so the van der Waals force is repulsive [32]. The total interaction force is repulsive for all separation distances. The colloid–wall and colloid–colloid interaction forces are shown in Fig. 10(b) and (c). These two interaction forces have resemblance in that they change from repulsive to attractive at separation distances of 0.175 nm and 0.871 nm, respectively.

3.2. Preliminary results of colloid trajectories near air–water interface

We now discuss some preliminary results of colloid trajectories near the air–water interface. The air front case is considered first. Fig. 11 shows 4 trajectories for colloids released at the locations near channel walls, but far away from the AWI. The locations for a time duration of 10.28 s after the release are shown, with time increment of 0.206 s. During this time duration, the colloids approach the AWI, travel toward the center, and then move away from the AWI near the center of the channel. The colloids essentially follow the flow streamlines as shown in the vector plot Fig. 9(a). Some minor fluctuations are observed due to the Brownian effect.

To gain some understanding of the relative magnitude of different forces, we compare in Fig. 12 the effective accelerations in x direction (the magnitude in y is similar) due to various forces for the #1 trajectory shown in Fig. 11. Fig. 12 (a) implies that

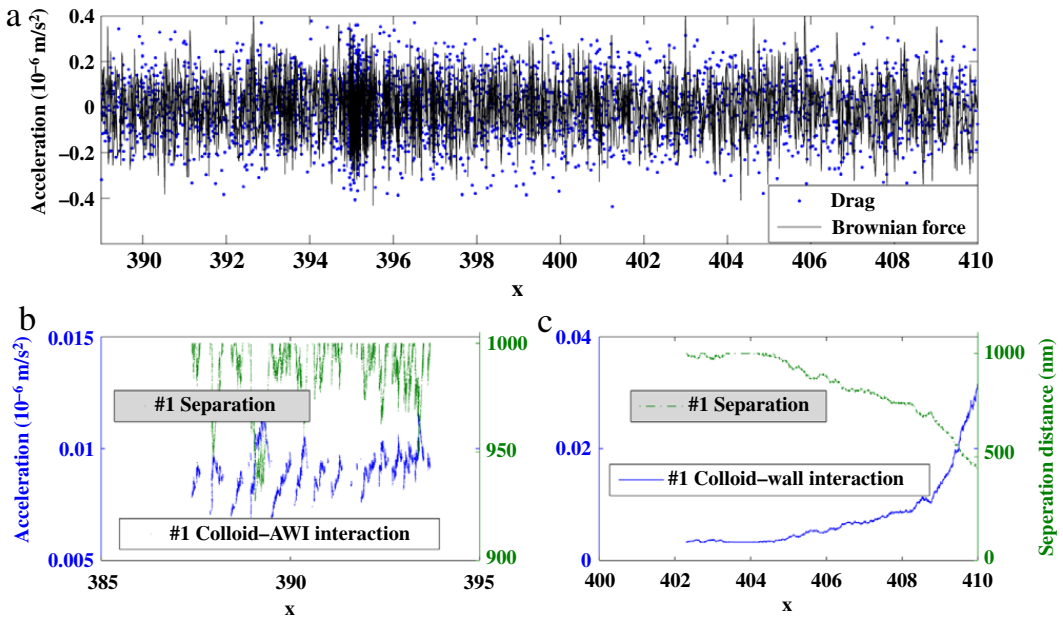

Fig. 12. The magnitudes of acceleration induced by various forces for Colloid #1 shown in Fig. 11: (a) drag and Brownian force as a function of streamwise location, (b) the net colloid–wall interaction force, (c) the net colloid–AWI interaction force.

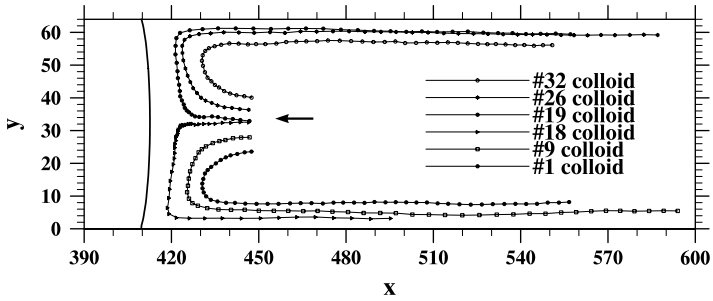

Fig. 13. Simulated colloid trajectories for the water front case.

the drag and Brownian forces are comparable, with a magnitude much larger than colloid–AWI (Fig. 12(b)) and colloid–wall (Fig. 12(c)) interaction forces. Note that the colloidal forces are calculated only when $h < 1$ μm. Initially, the colloid is very close to the wall and experiences wall interaction force. This wall interaction force becomes smaller as the colloid shifts away from the wall due to the net repulsive force. The colloid appears to reach a stable distance and then moves parallel to the wall towards the AWI. When the colloid trajectory bends near the AWI, a low-magnitude colloid–AWI interaction force exists, as shown in Fig. 12(b).

Fig. 13 shows 6 simulated trajectories for the water front case. The colloids are released at a same x location near the center of the channel. The time duration of the simulation is 25.7 s and the time increment for the position plot is 0.514 s or 10,000 dt. All the colloids move towards the AWI, turn before reaching the AWI, and then turn again near the wall and travel away from the AWI. It is important to note that different colloids take different times to make the turns. The closer to the center the initial location is, the longer it takes for the colloid to be deflected back. The colloid #18, for example, moves very close to the stagnation point at the center of the AWI. It may appear temporally trapped by the AWI, but it eventually escapes from the stagnation point.

This slow movement near the flow stagnation is also shown in Fig. 14, when the coordinates of colloid #18 and colloid #9 are shown as a function of time. While colloid #9 turns around very quickly, colloid #18 moves very slowly from time step 180 K to time step 380 K. This corresponds to a duration about 10 s of very slow movement.

Finally, we show in Fig. 15 the schematic colloid trajectories relative to the AWI, obtained from experimental visualization by a confocal microscope [9]. In the experiment, the channel cross-section has a trapezoidal shape. The mean interface velocity, determined from the confocal images, for water front (bottom) is 6.05 μm/s, and for air front (top) it is 4.62 μm/s. Note that the shapes of the AWI are similar to those in Figs. 4 and 8. The contact angles cannot be measured precisely based on the images, but their estimates are in rough agreement with the average literature values of 79 and 53 degrees for the water and air fronts, respectively [33–35]. The estimate for the air front in Fig. 15(a) is 51 degrees, and for the water front in Fig. 15(b), it is around 71.5 degrees.

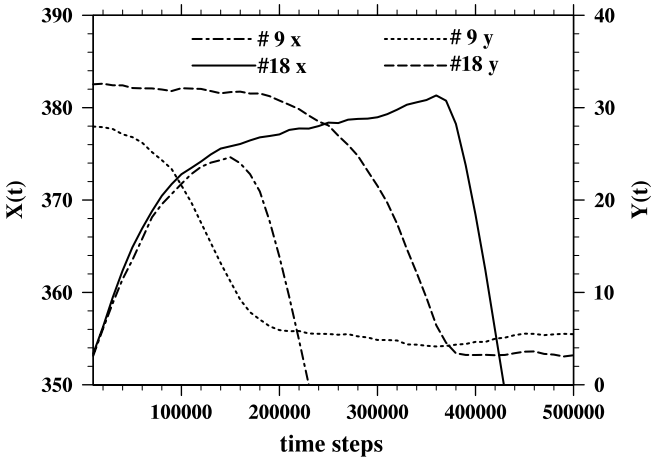

Fig. 14. Locations as a function of time for colloid #18 and colloid #26 shown in Fig. 13.

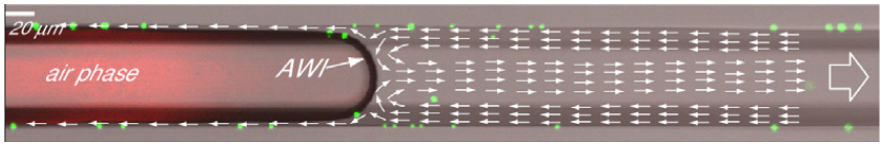

(a) Air front.

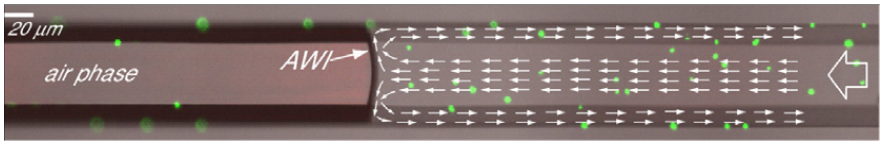

(b) Water front.

Fig. 15. Schematic colloid trajectories relative to AWI (shown with small arrows), obtained from experimental visualization by a confocal microscope [9]. The large arrows on the right end show the direction of the overall flow and the AWI. The particles shown in green are fluorescent microspheres and can be visualized in this experiment because of their fluorescent properties (and not because of their size). Due to the intense fluorescent signal from the particles, in the image they appear much bigger than their actual size.

The trajectories shown in Fig. 15 are very similar to what are shown in Figs. 11 and 13. These again show that the trajectories follow closely the flow streamlines. The difference in the experiment for the air front case is the trapped liquid near the bottom corner of the trapezoidal channel. Colloids are found to be retained in this corner region [9], but our 2D simulation cannot treat this fluid trapping.

4. Conclusions and summary

In this paper, we describe our approach to simulate multiphase viscous flow and colloid transport in a confined channel. We demonstrate that different computational approaches can be used to simulate a microfluidic multiphase flow at low capillary number. The lattice Boltzmann method and the volume-of-fluid interface tracking method can both be used to model fluid flow near a fluid–fluid interface. Both the contact angle and the relative flow pattern depend on the direction of the mean flow, in agreement with previous observations and our parallel micromodel visualizations [9].

Each method has its own advantages and disadvantages. The LBM is better suited for multiphase flows as the mesoscopic particle interaction defines the macroscopic contact angle, but simulating multiphase flows with large density ratio remains to be a challenge. Use of other forms of Equation of State in LBM may improve numerical stability and reduce spurious currents, as demonstrated in [20] for single-component multiphase LBM models. It is not clear whether the same can be applied to multicomponent multiphase LBM. The VOFIT requires explicit modeling of the moving contact line, but may be computationally more stable. In general, better algorithms are need to reduce spurious currents in both methods.

The Lagrangian tracking of colloids shows that the trajectories are mostly governed by the curved flow streamlines near the AWI, as seen in our micromodel experiment [9]. The simulation reported here is for a de-ionized solution with the repulsive electrostatic force dominating the colloid–surface and colloid–AWI interactions. Other solutions with different surface and colloid properties can be considered in the similar framework to study colloid retention. Other future work will include the modification of drag due to local hydrodynamic interaction and capillary interaction forces when a colloid is brought in contact with an interface [36]. 3D interfacial flow simulation in a trapezoidal channel may also be performed, following the work of Kang et al. [16].

Acknowledgements

This study is supported by the US Department of Agriculture (NRI-2006-02551, NRI-2008-02803), US National Science Foundation (ATM-0527140), and National Natural Science Foundation of China (Project No. 10628206). LPW acknowledges the travel support provided by ICMMES-08 through the NSF grant BET 0827259. We thank Professor Stéphane Zaleski of Université Pierre et Marie Curie, France for making his VOFIT code available to us. The kind help from Dr. Bogdan Rosa with the NCL graphics is acknowledged.

References

[1] J.F. McCarthy, J.M. Zachara, Subsurface transport of contaminants, Environ. Sci. Technol. 23 (1989) 496–502.
[2] J.E. Saiers, J.N. Ryan, Introduction to special section on colloid transport in subsurface environments, Water Resour. Res. 42 (2006) W12S01. doi:10.1029/2006WR005620.
[3] L.C. Goldenberg, I. Hutcheon, N. Wardlaw, Experiments on transport of hydrophobic particles and gas bubbles in porous media, Transport Porous Med. 4 (1989) 129–145.
[4] J. Wan, J.L. Wilson, T.L. Kieft, Influence of the gas-water interface on transport of microorganisms through unsaturated porous media, Appl. Environ. Microbiol. 60 (1994) 509–516.
[5] M. Auset, A.A. Keller, F. Brissaud, V. Lazarova, Intermittent filtration of bacteria and colloids in porous media, Water Resour. Res. 41 (2005) W09408. doi:10.1029/2004WR003611.
[6] J.T. Crist, J.F. McCarthy, Y. Zevi, P. Baveye, J.A. Throop, T.S. Steenhuis, Pore-scale visualization of colloid transport and retention in partly saturated porous media, Vadose Zone J. 3 (2004) 444–450.
[7] V. Lazouskaya, Y. Jin, Colloid retention at air–water interface in a capillary channel, Colloids Surf. A 325 (2008) 141–151. doi:10.1061/j.colsurfa.2008.04.053.
[8] J.E. Saiers, G.M. Hornberger, D.B. Gower, J.S. Herman, The role of moving air–water interfaces in colloid mobilization within the vadose zone, Geophys. Res. Lett. 30 (2003) 2083. doi:10.1029/2003GL018418.
[9] V. Lazouskaya, L.-P. Wang, H. Gao, X. Shi, K. Czymmek, Y. Jin, Pore-scale investigation of colloid transport and retention in the presence of dynamic air–water interface, Vadose Zone J., 2008 (submitted for publication).
[10] S. Chen, G.D. Doolen, Lattice Boltzmann method for fluid flows, Annu. Rev. Fluid Mech. 30 (1998) 329–364.
[11] R. Scardovelli, S. Zaleskii, Direct numerical simulation of free-surface and interfacial flow, Annu. Rev. Fluid Mech. 31 (1999) 567–603.
[12] J.A. Sethian, P. Smereka, Level set methods for fluid interfaces, Annu. Rev. Fluid Mech. 35 (2003) 341–372.
[13] M. Gorokhovski, M. Herrmann, Modeling primary atomization, Annu. Rev. Fluid Mech. 40 (2008) 343–366.
[14] Q. Kang, D. Zhang, S. Chen, Displacement of a two-dimensional immiscible droplet in a channel, Phys. Fluids 14 (2002) 3203–3214.
[15] Q. Kang, D. Zhang, S. Chen, Immiscible displacement in a channel: Simulations of fingering in two dimensions, Adv. Water Resources 27 (2004) 13–22.
[16] Q. Kang, D. Zhang, S. Chen, Displacement of a three-dimensional immiscible droplet in a duct, J. Fluid Mech. 545 (2005) 41–66.
[17] X. Shan, H. Chen, Lattice Boltzmann model for simulation flows with multiple phases and components, Phys. Rev. E 47 (1993) 1815–1819.
[18] X. Shan, H. Chen, Simulation of nonideal gases and liquid-gas phase transitions by the lattice Boltzmann equation, Phys. Rev. E 49 (1994) 2941–2948.
[19] X. Shan, Analysis and reduction of the spurious current in a class of multiphase lattice Boltzmann models, Phys. Rev. E. 73 (2006) 047701.
[20] Y. Peng, L. Schaefer, Equations of state in a lattice Boltzmann model, Phys. Fluids. 18 (2006) 042101.
[21] X. Shan, G.D. Doolen, Diffusion in a multicomponent lattice Boltzmann equation model, Phys. Rev. E. 54 (1996) 3614–3620.
[22] C. Chang, C.H. Liu, C.-A. Lin, Boundary conditions for lattice Boltzmann simulations with complex geometry flows, ICMMES2007 Proceedings.
[23] D. Gueyffier, J. Li, A. Nadim, R. Scardovelli, S. Zaleski, Volume-of-fluid interface tracking with smoothed surface stress methods for three-dimensional flows, J. Comput. Phys. 152 (1999) 423–456.
[24] M. Renardy, Y. Renardy, J. Li, Numerical simulation of moving contact line problems using a volume-of-fluid method, J. Comput. Phys. 171 (2001) 243–263.
[25] M. Seifollahi, E. Shirani, N. Ashgriz, An improved method for calculation of interface pressure force in PLIC-VOF methods, Euro. J. Mech. B-Fluids 27 (2008) 1–23.
[26] R.G. Cox, The dynamics of the spreading of liquids on a solid surface. Part 1. Viscous flow, J. Fluid Mech. 168 (1986) 169–194.
[27] M.J. Elimelech, J. Gregory, X. Jia, R.A. Williams, Particle Deposition and Aggregation: Measurement, Modeling, and Simulation, Butterworth-Heinemann, Oxford, 1995.
[28] R.H. Yoon, L. Mao, Application of extended DLVO theory, IV, J. Colloid Interface Sci. 181 (1996) 613–626.
[29] R.H. Yoon, D.H. Flinn, Hydrophobic interactions between dissimilar surfaces, J. Colloid Interf. Sci. 185 (1997) 363–370.
[30] J. Gregory, Approximate expressions for retarded van der Waals interaction, J. Colloid Interface Sci. 83 (1981) 138–145.
[31] V. Lazouskaya, Y. Jin, D. Or, Interfacial interactions and colloid retention under steady flows in a capillary channel, J. Colloid and Interf. Sci. 303 (2006) 171–184.
[32] S.A. Bradford, S. Torkzaban, Colloid transport and retention in unsaturated porous media: A review of interface-, collector-, and pore-scale processes and models, Vadose Zone J. 7 (2008) 667–681.
[33] H.Y. Erbil, G. McHale, S.M. Rowan, M.I. Newton, Determination of the receding contact angle of sessile drops on polymer surfaces by evaporation, Langmuir 15 (1999) 7378–7385. doi:10.1021/la9900831.
[34] H. Lim, Y. Lee, S. Han, J. Cho, K.-J. Kim, Surface treatment and characterization of PMMA, PHEMA, and PHPMA, J. Vac. Sci. Technol. A 19 (2001) 1490–1496.
[35] H. Kaczmarek, H. Chaberska, The influence of UV-irradiation and support type on surface properties of poly(methyl methacrylate) thin films, Appl. Surf. Sci. 252 (2006) 8185–8192. doi:10.1016/j.apsusc.2005.10.037.
[36] P.A. Kralchevsky, K. Nagayama, Capillary interactions between particles bound to interfaces, liquid films and biomembranes, Adv. Colloid Interface Sci. 85 (2000) 145–192.